https://doi.org/10.5194/egusphere-2026-4298
Preprint. Discussion started: 11 August 2026

Rayleigh-wave focal spot imaging of the polymetallic Kylylahti mine area in the Outokumpu mineral district, Finland

Christina Tsarsitalidou[1,2,★], Valtteri Hopiavuori[1,★], Kauri Kolehmainen[1], Gregor Hillers[1], Yang Lu[1], Suvi Heinonen[1], Michal Malinowski[3], Pierre Boué[4], Bruno Giammarinaro[5], Laurent Stehly[4], and Kari Komminaho[1]

[1]Institute of Seismology, University of Helsinki, Helsinki, Finland
[2]Now at Geosciences Barcelona (GEO3BCN), CSIC, Barcelona, Spain
[3]Geological Survey of Finland, Espoo, Finland
[4]Institut des Sciences de la Terre, Université Grenoble Alpes, Grenoble, France
[5]LabTAU, INSERM, Centre Léon Bérard, Université Claude Bernard Lyon 1,Lyon, France
[★]These authors contributed equally to this work.

Correspondence: Christina Tsarsitalidou (christina.tsarsitalidou@helsinki.fi)

Abstract. The green energy transition requires the development of new seismic imaging approaches to locate and characterize deposits of critical raw materials efficiently and cost-effectively. Here, we apply the Rayleigh-wave focal spot imaging approach to dense array data collected in the Kylylahti polymetallic mine area in the Outokumpu mineral district, Finland, and demonstrate the efficiency of the method in a hardrock environment. We cross-correlate one month of ambient-noise records from the 994 vertical-component stations deployed over an area of $\sim$10.5 km^2 following standard signal processing operations. The anatomy of the correlation wavefield includes spurious arrivals associated with the local mining operations and with a mine located to the SW of the array. From the narrow-band zero lag amplitude distribution of the cross-correlations we get the Rayleigh-wave focal spots which we parameterize with a Bessel-function model to estimate the local phase velocity at each station. The employed model accounts for the anisotropic background illumination and is constrained using focal spot data in the short 1λ distance range. In the $3-6$ Hz frequency range we obtain phase velocity maps that correlate well with the Kylylahti formation, which is resolved with lower phase velocity values compared to the host rock. The lower phase velocities are associated with abundant soapstone, while higher phase velocities are indicative of the surrounding mica schist. The similarity of the phase-velocity features to the structure resolved by an independently obtained P-wave velocity model, together with the agreement between the inferred Kylylahti formation boundaries and the contours of the geological model, suggest that the focal spot method is a valuable, low-cost passive imaging tool for modern mineral exploration that can complement established approaches.

1 Introduction

The growing demand for critical raw materials for the low-carbon energy transition requires efficient and sustainable mineral exploration strategies (Alcalde et al., 2022). Seismic ambient noise dense array imaging offers a cost-effective and environmentally low-impact method for a wide range of spatial scales, providing a convenient method for exploration in challenging

https://doi.org/10.5194/egusphere-2026-4298
Preprint. Discussion started: 11 August 2026

and sensitive environments. Seismic ambient noise is largely dominated by surface-wave energy, hence noise-based imaging applications mainly utilize dispersive surface waves. The dispersive nature of the waves is translated into shear-wave velocity images of the subsurface structures. This has led to various applications of passive surface-wave tomography in mineral exploration, including the identification of contacts between a mineralization-hosting formation and the surrounding rock (Da Col et al., 2020), fault zones and structures associated with mineralization (Ryberg et al., 2022; Wilczynski et al., 2024), and the continuation of known deposits (Colombero et al., 2022). Here we demonstrate that the dense array spatial autocorrelation contains complementary information to cross-correlation tomography for mineral exploration imaging.

Surface-wave focal spot imaging is an ambient-noise method for estimating local medium properties using dense seismic arrays. The method analyzes the shape of the focal spot, which is the large amplitude feature around the reference station at zero-lag time ($\tau = 0$ s) in the seismic noise correlation wavefield. It appears because time-domain cross-correlations of diffuse ambient noise reconstructs the wavefield between receivers, thus yielding an estimate of the Green's function between them (e.g., Derode et al., 2003a, b). The causal ($\tau > 0$ s) and acausal ($\tau < 0$ s) parts of the Green's function correspond to diverging and converging waves in the correlation wavefield that emerges from the correlation process (Wapenaar et al., 2010). At zero lag, when these waves are superimposed, they form the focal spot. The narrow-band zero-lag cross-correlation amplitude distribution is the time-domain equivalent of the frequency-domain spatial autocorrelation (SPAC) (Aki, 1957; Tsai and Moschetti, 2010). This equivalence allows focal spots to be parametrized using the same models obtained for SPAC and its extension (Haney et al., 2012).

Focal spots were first studied in ultrasound time-reversal experiments (Fink, 1999) and were later adopted in medical imaging and ambient-noise seismology (Catheline et al., 2008; Hillers et al., 2016). Using synthetic experiments Giammarinaro et al. (2023) and Giammarinaro et al. (2024) showed that the method can resolve lateral structures that are smaller than the wavelength, and that it can provide better depth resolution than the more widely used ambient-noise tomography. The increase in depth sensitivity was demonstrated by Tsarsitalidou et al. (2024) using seismic data from the continental scale USArray. Tsarsitalidou et al. (2026) constructed the first 3D shear-wave velocity model based on AlpArray focal spot observations, which was supported by a parametrization that corrects for the anisotropic background illumination (Haney et al., 2012). This demonstrates the effectiveness of the method in an environment with directional wave incidence.

The Kylylahti mining area is located in the northwestern part of the Outokumpu mineral district in Eastern Finland. It has been the focus of geological and geophysical studies due to its polymetallic (Cu–Co–Zn–Ni–Ag–Au) semi-massive to massive ore deposit, which were actively mined from 2012 to 2020. In recent years, the area has served as a case study for the development of advanced geophysical techniques for mineral exploration. In particular, the Cost-effective Geophysical Imaging Techniques for supporting Ongoing Mineral exploration in Europe (ERA-MIN COGITO-MIN) project (Koivisto et al., 2018), launched in 2016, acquired and analyzed passive (Chamarczuk et al., 2019a, b, 2021, 2022) and active seismic data from the surface (Heinonen et al., 2019; Singh et al., 2019) and boreholes (Riedel et al., 2018) in the area. These studies demonstrate that the complex geology of the Kylylahti area, particularly the steeply dipping geological contacts, challenges imaging with surface seismic reflection methods.

https://doi.org/10.5194/egusphere-2026-4298
Preprint. Discussion started: 11 August 2026

The extensive research history of the study site provides a valuable benchmark for validating our results as we investigate, for the first time, the effectiveness of the passive surface-wave focal spot imaging method for resolving near surface structures in the context of mineral exploration.

We apply the focal spot method to the Kylylahti dense array dataset, which was recorded using an active survey design that was not optimized for the method. The location of the then-active Kylylahti mine inside the array boundary poses an additional imaging challenge because the mining activity acts as a major source of noise, which can lead to spurious arrivals in the reconstructed wavefield. We use 30-days-long ambient-noise seismic records acquired by the COGITO-MIN-project to investigate the seismic ambient-noise field of the Kylylahti area and perform a focal spot analysis to produce phase velocity maps that characterize the geological features of the study site. Following Tsarsitalidou et al. (2026), we apply Bessel functions modeled for anisotropic background illumination to mitigate biasing effects associated with directional surface-wave energy. We cluster dispersion curves obtained from the focal spot analysis (Tsarsitalidou et al., 2024), and show that the resulting clusters approximate geologically similar features of the study area. We validate our imaging results by comparing them to an independently obtained travel time tomography model (Singh et al., 2019) and to the geological model provided by the mining company Boliden, which is constrained by extensive drill-hole data, geological observations, and geophysical interpretations. Our results demonstrate that focal spot imaging is a robust passive seismic imaging tool for characterizing subsurface velocity structures at hardrock sites under non-optimal conditions. As a result, it provides a relatively low-cost and logistically less challenging approach for mineral exploration compared to active seismic surveys.

In this article, we first introduce the geology of the Kylylahti area, provide background information about the data acquisition, and analyze the anatomy of the wavefield (Sect. 2). This is followed by an overview of the anatomy of the correlation field (Sect. 3). In Section 4, we describe the anisotropic focal spot imaging method. In Section 5, we present our results, which include detailed representation of selected individual focal spots, dispersion curve clusters, and phase velocity maps. In Section 6, we discuss the performance of the focal spot imaging in the Kylylahti mining area, interpret the obtained frequency dependent phase-velocity structure in the context of the known geology and compare our results with the seismic tomography model of Singh et al. (2019). We examine the wavefield anatomy and its effect on the imaging resolution.

2 Data

2.1 Geological setting

The Kylylahti massif in the Outokumpu mineral district in Eastern Finland (Fig. 1) contains a polymetallic (Cu-Co-Zn-Ni-Ag-Au) semi-massive to massive sulphide deposit. According to Peltonen et al. (2008), the massif is characterized by multiphase deformation, a tight synformal fold structure and shear faulting. The sulphide deposit is located at its eastern margin and is associated with ultramafic rocks, mainly serpentinite and soapstones (talc-carbonate rocks), and surrounding alteration zones composed of carbonate-skarn-quartz rocks. The massif (hereafter referred to as Kylylahti formation) trends nearly N-S and occurs as a near-vertical body within the Kaleva sedimentary belt, consisting mainly of mica schist and black schist. The

https://doi.org/10.5194/egusphere-2026-4298
Preprint. Discussion started: 11 August 2026

sulphide deposit occurs along steeply dipping contacts between black schists and carbonate–skarn–quartz rocks as steeply dipping sulphide lenses and disseminated mineralization zones.

2.2 Data acquisition, array configuration, and ambient seismic wavefield conditions

During the COGITO-MIN project, a seismic array with 994 stations recorded ambient noise for 600 hours between August and September 2016, for 20 hours per day. The array was designed using 19 receiver lines with 200 m spacing and 50 m in-line receiver spacing (Fig. 1). The array spread over 10.5 km^2 with surface conditions ranging from exposed bedrocks to swampy conditions. Each station consisted of tightly colocated six 10 Hz vertical component geophones connected to a wireless datalogger that recorded ambient noise at 2 ms or 500 Hz (Chamarczuk et al., 2019a).

The target area hosted multiple anthropogenic noise sources. The most dominant was the Kylylahti mine itself which was active during the deployment. Mining-related noise included scheduled blasts, scaling, vehicle activity, and airwaves generated by the ventilation system (Chamarczuk et al., 2019a, b). Additional noise sources originated from roads, the town of Polvijärvi (Fig. 1), and a distant open-pit mine to the SW. During the deployment, the array recorded controlled sources from the COGITO-MIN active survey, which included both explosive and vibroseismic sources. The active survey was carried out over 13 non-consecutive days between 15 August and 8 September 2016, with typical data acquisition periods between early morning and early evening. The ambient wavefield was dominated by surface waves, largely associated with repetitive mining activity, although significant body-wave energy was also present due to both mining operations and the COGITO-MIN survey (Chamarczuk et al., 2019a, b).

2.3 Preprocessing and noise correlations

We preprocess the vertical-component data implementing standard signal processing operations for passive noise correlation surface-wave tomography. We adapt the workflow of Tsarsitalidou et al. (2024) and Tsarsitalidou et al. (2026) to the higher frequency Rayleigh waves studied with the 3.5×3 km^2 Kylylahti array. Similar to Chamarczuk et al. (2022), we remove the active-source data from the continuous records. We reorganize the receiver gathers to daily records, apply a $0.2 - 40$ Hz bandpass filter and decimate to 125 Hz. We cut the daily records into 1 hr segments and normalize the amplitude first in the frequency domain using spectral whitening between 0.2 to 40 Hz, and then in the time-domain by clipping the amplitude at three times the standard deviation of the signal distribution in each 1 hr window. We implement tapering to prevent spectral leakage. We cross-correlate the 1 hr time-window data and stack the correlations linearly. The 30 s maximum lag time is sufficiently long for filtering the cross-correlations in the target frequency range of $3 - 6$ Hz.

We apply a narrow-band Gaussian filter to target the center frequencies of the dispersion measurements in the range $3-6$ Hz with a step size of 0.25 Hz. The filter follows similar focal spot imaging applications (Giammarinaro et al., 2023; Tsarsitalidou et al., 2024), and is defined as $h(\omega) = \exp(-\alpha(\frac{\omega - \omega_c}{\omega_c})^2)$, where $\alpha = 1000$ and ω_c is the central angular frequency of the Fourier transform of the cross-correlation.

https://doi.org/10.5194/egusphere-2026-4298
Preprint. Discussion started: 11 August 2026

3 Anatomy of the correlation field

We assess the characteristics of the ambient-noise field and identify the dominant noise sources in the Kylylahti area using our seismic interferometry results in the $3-6$ Hz frequency range, which shows the best signal-to-noise ratio relevant for the focal spot imaging analysis. Ambient-noise tomography as well as the spatial autocorrelation imaging used here are based on the cross-correlation of seismic noise recorded at two stations, which provides an empirical estimate of the Green's function (Wapenaar et al., 2010). When Green's functions are calculated between all array stations and a selected reference station, the resulting correlation wavefield represents the response to a virtual seismic source at the reference site. The dynamics of the 2D surface-wave component are equivalent to a time-reversal field (e.g., Derode et al., 2003a, b). For negative time lags, the wavefield converges towards the reference station, forms the focal spot at time $\tau = 0$ s, and then diverges like the wavefront excited by the virtual point source at positive time lags. This behavior is expected for diffuse and for multiple scattered wavefield conditions. However, if repetitive or persistent noise sources are located in the target region, these assumptions are violated, and spurious arrivals emerge that are not parts of the interstation Green's function.

The correlation field of the Kylylahti area is complex. In addition to the Green's function arrivals it also contains signals associated with coherent sources located inside and outside the array. Figure 2 shows time lapse impressions of the $3-6$ Hz broadband correlation wavefields associated with two reference stations indicated by the red stars. In both fields, the strongest and most coherent energy is associated with the virtual source, i.e., the diverging wavefield (DW) component at positive lag times. At negative lag times, however, a coherent near-planar wave front (PW) propagates across the array from the SW to NE, which is associated with energy excited at the open-pit mine (Chamarczuk et al., 2019b) located $\sim$5 km away to the SW. This wave front is stronger than the weaker converging part of the surface-wave Green's function that is consequently not resolved in these amplitude distributions. In both correlation wavefields a relatively slowly propagating signal (AW) can be discerned that is excited within the array at the eastern boundary of the mining area. The speed of $\sim$330 m/s identifies it as an airwave that is generated by the mine ventilation system (Chamarczuk et al., 2019b). It is one of the most persistent noise sources in the target area during the acquisition. It is emitted at $\tau = -2.5$ s and -3.7 s relative to the stations 516 and 1029, respectively, that are located $\sim$850 m and $\sim$1200 m away from the airwave origin, illustrating again the $\sim$330 m/s propagation speed.

Mining activity excites Rayleigh waves (SW) at the eastern and western sides of the mine, and the reconstructed amplitude patterns are strongly sensitive to the reference location ($\tau = -0.31$ s). E.g., only the eastern Rayleigh-wave signal contributes to the correlation field of station 516 (top row), whereas both signals contribute to the field of station 1029 (bottom row). Consistent with isolated source effects at the local scale (Yang et al., 2022; Schippkus et al., 2022; Li et al., 2025), we identify the active mine area as a strong near-field source region that produces spurious arrivals that break the lag time symmetry of the obtained cross-correlations, and that are not part of the Green's function. We demonstrate, however, that the obtained focal spot images are not controlled by these excitation patterns but contain genuine information about the structure of the propagation medium. Note that the broadband refocusing pattern at $\tau = 0$ s approximates the theoretical delta-function impulse and thus differs from the narrow-band focal spots shown in Fig. 3a.

https://doi.org/10.5194/egusphere-2026-4298
Preprint. Discussion started: 11 August 2026

4 Focal Spot Imaging

Again, the focal spot is the narrow-band zero-lag time amplitude distribution of the cross-correlation field. It is the time-domain equivalent of the spatial autocorrelation or SPAC formulated in the spectral domain (Aki, 1957; Tsai and Moschetti, 2010), and as such related to the imaginary part of the Green's function (Sánchez-Sesma and Campillo, 2006). Implementing focal spot imaging means estimating local dispersion curves at every station location through the parameterization of focal spots with Bessel-function models developed under the SPAC framework (Aki, 1957). The SPAC method has been frequently used in near-surface imaging and geotechnical engineering (Okada and Suto, 2003; Foti et al., 2018; Hayashi et al., 2022; Asten and Hayashi, 2018), where dispersion curves are estimated directly from measurements acquired with specifically designed concentric arrays at the local scale. It has also been used to estimate surface-wave phase velocities at the continental scale as part of a workflow that includes a tomographic inversion to image velocity variations locally (Ekström, 2014; Kästle et al., 2018). Our dense array approach differs from both applications. We apply it to data from large-N arrays that offer dense spatial sampling related to the wavelength to estimate local dispersion at individual station locations using data from a short distance range. Thus, in contrast to tomography, the location of each array station is a spatial sample, although at the shorter wavelengths not all array stations contribute to the model regression (Hillers et al., 2016; Tsarsitalidou et al., 2024). The phase velocity images are compiled iteratively without solving a tomographic inverse problem, and uncertainty estimates can also be obtained locally. This has the potential for a better control of the lateral resolution through choices of the data distance range (Giammarinaro et al., 2023, 2024; Tsarsitalidou et al., 2024) or by the application of image enhancement techniques (Kolehmainen et al., 2025).

In a USArray focal spot imaging application, Tsarsitalidou et al. (2024) estimated the Rayleigh-wave phase velocity using the classic SPAC models under the assumption of isotropic illumination (Aki, 1957; Haney et al., 2012), which are the simple J_0 and J_1 functions for the ZZ and ZR (and RZ) components, respectively. In an AlpArray application (Tsarsitalidou et al., 2026), the employed Bessel-function parametrization is adjusted for the anisotropic background illumination (Nakahara, 2006; Haney et al., 2012) at every period. Here, too, we perform this focal spot parameterization (Tsarsitalidou et al., 2026) using a Bessel-function model adapted to the directional surface-wave incidence that can vary at the location of each station across the frequency range. The model for the ZZ-component is (Nakahara, 2006; Haney et al., 2012)

$$C(r,\psi) = a_0 J_0(kr) + \sum_{m=1}^{M-1} j^m J_m(kr)\big(a_m \cos(m\psi) + b_m \sin(m\psi)\big), \tag{1}$$

where the a_m and b_m are amplitude coefficients, j is the imaginary unit, ψ is the azimuthal angle between the reference and a target station, and J_m is a Bessel function of the first kind of order m. The summation index starts at m=0, resulting in the a_0 term, and counts up to $M-1$. M is the number of the correction terms that depends on the wavenumber k and the data range r_{fit} (Seydoux et al., 2017). Only the real part of Eq. (1) is used for the focal spot parameterization. Using $r_{\text{fit}}=1\lambda$ results in $M = k_{\text{ang}} r_{\text{fit}} = \frac{2\pi}{\lambda} 1\lambda \approx 6.3$, where$k_{\text{ang}}$ is the angular wavenumber. Thus, Eq. (1) becomes Eq. (2) for M=6,

$$A(r,\psi,\tau=0) = \sigma J_0(kr) - J_2(kr)\big(a_2\cos(2\psi) + b_2\sin(2\psi)\big) + J_4(kr)\big(a_4\cos(4\psi) + b_4\sin(4\psi)\big). \tag{2}$$

https://doi.org/10.5194/egusphere-2026-4298
Preprint. Discussion started: 11 August 2026

The isotropic Rayleigh-wave phase velocity is estimated from fitting Eq. (2) to the Gaussian filtered focal spots at every frequency. The free parameters are the Bessel-function argument wavenumber k, from which the phase velocity c_R is estimated, the amplitude factor σ, and the coefficients a_2, b_2, a_4, b_4.

The phase velocity is estimated similar to the iterative procedure developed by Tsarsitalidou et al. (2026). We apply this three-step nonlinear regression to the narrow-band focal-spot data to estimate k, σ, and the a_m and b_m coefficients. In the first step, we fit the isotropic SPAC model $\sigma J_0(kr)$ using data points from all distances r, and estimate k_1 and σ_1. In the second step, we fit the anisotropic model in Eq. (2) to data at $r \leq r_{\text{fit}} = 1\lambda$, using $M = k_1 r_{\text{fit}} = 6$. The free parameters are k_2 and σ_2 and the weights $a_{2,4}$ and $b_{2,4}$. We then scale the data by σ_2 and perform a third regression with the same anisotropic model, keeping the wavenumber fixed $k_2 = k_3$. After this final iteration, σ_3 equals unity, which supports properly normalized residual-sum-of-squares (RSS) estimates.

After the third iteration, the RSS parameter is estimated that represents a quality control measure of the regression. The RSS is also used to estimate the standard error ε_k,

$$\varepsilon_k = \sqrt{\frac{\text{RSS}}{\text{dof}} \cdot C_k}, \tag{3}$$

where C_k and dof are the element of the covariance matrix associated with k, and the degrees of freedom, respectively. We apply this algorithm to narrow-band focal spots reconstructed at every array station. That way we obtain 994 dispersion curves with phase velocity measurements in the $3-6$ Hz range sampled with an interval of 0.25 Hz. The target frequency range is typically constrained by the shortest and longest wavelengths, which are estimated from the interstation distance and the array aperture, respectively. In this study, however, frequencies below 3 Hz are excluded because the anisotropic noise wavefield at near-field distances leads to velocity estimates that are clearly biased by the mine activity. At frequencies above 6 Hz, the velocity maps no longer exhibit coherent features.

5 Results

5.1 Focal spots

Figure 3a illustrates 4 Hz focal spots reconstructed at three station located in the NW, SW, and SE of the array, together with the best-fitting Bessel-function model used to estimate the velocity (Fig. 3b) and the residuals (Fig. 3c). The inset in each panel shows the associated amplitude distance dependence of the amplitudes. From the focal spot shape we can infer the direction of the strong anisotropic wavefield incidence, which is highly heterogeneous across the Kylylahti array. At the NW location in the mine area indicated by the cyan contour, we observe a strong incidence in the EW direction that is probably linked to the mine activity. For the two station locations in the South, the short axis of the oval-shaped focal spots that is indicative of the dominant flux direction (Giammarinaro et al., 2023) points to the center of the array. For the SW station, this can be influenced by the distant mine activity or by local traffic considering the roundabout of a regional road that is located at the center of the array. Together with the connecting roads this has been discussed as a relevant source of ambient-noise generation

https://doi.org/10.5194/egusphere-2026-4298
Preprint. Discussion started: 11 August 2026

(Chamarczuk et al., 2022). Overall, these observations illustrate the general behavior of the surface-wave incidence directions across the array that suggest the mine area in the NW is a dominant noise source.

Another important feature is the focal spot coda pattern at long distances from the center beyond the first zero crossing. This is particularly evident for the two stations in the South, where the coda amplitudes do not follow a circular pattern indicative of a relatively homogeneous medium as observed in the continental scale focal spot applications (Tsarsitalidou et al., 2024, 2026). Instead the coda shape appears to be affected by the highly heterogeneous medium, similar to the focal spot coda patterns in a fault zone environment obtained by Hillers et al. (2016).

The spatially variable best-fitting Bessel-function models described in Eq. (2) are shown in Fig. 3b. As expected, the model reflects the corresponding focal spot shape in Fig. 3a, and corroborates the anisotropic incidence. The associated 1D representations exhibit distance-dependent amplitude features that vary from station to station. These variations reflect the station spacing and the spatial heterogeneity of the ambient-noise wavefield across the array. For stations 1318 and 1550 (center and right column), the residual distributions, defined as the difference between the model and the focal spot data, indicate the presence of body-wave energy. Across the considered distance range of 1λ, the model systematically underestimates the focal-spot amplitudes, resulting in negative residual values. A similar effect was observed for long-period USArray focal spots influenced by body-wave energy generated by teleseismic earthquakes (Tsarsitalidou et al., 2024). In the present application, however, the body-wave energy in the target frequency range is associated to the underground mining activity (Chamarczuk et al., 2022). These body-wave effects can be mitigated using larger data ranges (Giammarinaro et al., 2023; Tsarsitalidou et al., 2024). Whereas we cannot exclude a small influence on the obtained phase velocity values, the consistency and coherency of our images suggest that this body-wave sensitivity does not govern our results. As indicated by the residual distribution for station 516 located on the western side of the mine (left column), the body-wave effect, too, varies spatially, which highlights again the complex and challenging wavefield anatomy in the target area.

5.2 Phase velocity maps

Figure 4a shows phase velocity maps for three frequencies between 4.5 and 5.5 Hz, together with the RSS estimates and standard error obtained for every dispersion measurement (Figs. 4b, c), as discussed in Sect. 4. In Figure 4d, we present the median filtered versions of the phase velocity maps in panel (a). For every frequency, we replace the phase velocity at a station location by the median value of the velocity estimates from that station and its four nearest neighbors, which in most cases are located inline of the station. In this way, we suppress small-scale fluctuations or artifacts that do not exhibit spatial coherence in their neighborhood, without degrading the lateral resolution.

Overall, in the $4.5-5.5$ Hz frequency range, the main feature observed in the phase velocity maps is a low-velocity zone located in the northern part of the array that expands toward the center at lower frequencies. By its position and shape this low-velocity area is associated with the Kylylahti formation, which outcrops in the northern part of the study area and dips southward, with its lower part reaching a depth of approximately 1.6 km. Geological mapping of the study area indicates an abundance of soapstones formed by alteration of serpentinite. These lithologies generally exhibit lower seismic velocities than the surrounding mica schist, with average values of 5540 $\mathrm{m\,s^{-1}}$ and 5630 $\mathrm{m\,s^{-1}}$, respectively (Luhta, 2018). Accordingly, mica

https://doi.org/10.5194/egusphere-2026-4298
Preprint. Discussion started: 11 August 2026

schist regions appear with average-to-high Rayleigh-wave phase velocity values. Another feature observed in the velocity maps is an elongated low-velocity zone a few hundred meters to the east of the Kylylahti formation. This lithological unit corresponds to a black schist unit (Peltonen et al., 2008) that exhibits lower average v_P velocities (5550 $\mathrm{m\,s^{-1}}$) than the surrounding mica schist (5630 $\mathrm{m\,s^{-1}}$) (Luhta, 2018), which explains its appearance in the velocity maps.

Overall, the RSS and standard error maps exhibit higher values at increasing frequencies, likely due to the smaller number of data points available in the 1λ distance range for the focal spot parameterization. High values in the corresponding error and RSS maps suggest that the assumption of a homogeneous medium underlying Eq. (2) is too simplistic for the complex imaging environment. Intriguingly, however, the distributions of these uncertainty estimates are not random. The dense spatial wavefield sampling and the employment of short data distances supports the resolution of line-shaped features that can be clearly distinguished from their surroundings. As observed before (Hillers et al., 2016; Tsarsitalidou et al., 2024), they indicate the interaction of the wavefield with scattering velocity contrasts that yield components in the spatial autocorrelations which are not compatible with the model assumptions. The fact that the uncertainty patterns reflect the geological structure and are not controlled by noise-source or body-wave distributions associated with the mining activities are a strong indicator of the robustness of the focal spot imaging approach.

5.3 Dispersion curve clustering

We implement a cluster analysis of the focal spot dispersion curves to recover the lithological boundaries that control the shape of the curves to guide our interpretations of the phase velocity spatial variability. We use the kmeans clustering method (Pedregosa et al., 2011) to group the dispersion curves into equal-variance groups by minimizing the sum of squares of the distances between each sample and a group centroid. The clustering algorithm is applied to the median filtered dispersion curves as explained in Sect.5.2.

Using the elbow method, we compute the total squared error of the clustering, called inertia, for a number of clustering groups that varies between 1 to 30, and find that the optimal number of clusters equals to three. While weak dispersion is observed in the studied frequency range, the three clusters shown in Fig. 5 are representative of the focal spot velocity estimation. Considering that the clustering algorithm is ignorant of the spatial relations of the processed dispersion curves, the spatial coherency of the obtained clusters suggests a dominant structural control of the results that was similarly observed at much larger scale and longer periods (Tsarsitalidou et al., 2024).

The orange indicated Cluster 1 represents the low velocity values associated with the Kylylahti formation in the north-central part of the array. The black dots in the figure inset illustrate the contour of a geological model at 150 m depth, in contrast to the surface geology traces used in previous figures, and which also correlates well with the dispersion curve Cluster 1 and the associated Kylylahti formation. The largest Cluster 2 includes most dispersion curves with intermediate velocities in our database. Cluster 3 indicates the high-velocity region in the SE corner of the array, which is distinguished from Cluster 2 by the high velocities for frequencies above 5 Hz. The resolution of high velocities in this area is consistent with previous v_P imaging results obtained using the first-arrival travel time tomography (Singh et al., 2019). However a slight velocity overestimation is anticipated as a consequence of the half focal spot parameterization, in which the majority of the data points are concentrated

https://doi.org/10.5194/egusphere-2026-4298
Preprint. Discussion started: 11 August 2026

along the major semi-axis that captures the strong wavefield incidence. The parameterization shifts the first zero crossing to longer distances, which leads to an overestimation of the apparent wavelength and thereby the phase velocity.

6 Discussion

In this study, we pilot the focal spot method in the Kylylahti mining area. Passive imaging in the study area is challenging because of the non-optimal survey design, and the several persistent noise sources located within the array that break the basic assumptions of seismic interferometry, affecting both the background illumination and the usable frequency range. Therefore, we estimate Rayleigh-wave phase velocity using 2D Bessel-function models that account for the directional incidence. Despite the challenges, our images resolve the most significant geological features in the area, which demonstrates the overall usefulness and convenience of focal spot imaging in mineral resources exploration.

Overall, the phase velocity maps and dispersion-curve clusters correlate with the dominant geological features. In Figure 4 the Kylylahti formation is observed at all frequencies as a low-velocity zone compared to its surroundings that are dominated by the faster mica schist. A similar observation can also be made in Fig. 5, where the dispersion-curve cluster corresponding to the lowest velocities is associated with the formation. The lower phase velocities are associated with abundant talc-bearing soapstones, which formed through alteration of serpentinite (Kontinen et al., 2006; Peltonen et al., 2008). Talc is a mechanically soft mineral with relatively low elastic moduli and extraordinarily high elastic anisotropy, with the degree of anisotropy decreasing as the pressure increases (Bailey and Holloway, 2000; Mainprice et al., 2008). Petrophysical P-wave measurements conducted by Luhta (2018) from Kylylahti drill core samples showed that soapstone, exhibit lowest mean P-wave velocities of all samples (5540 $\mathrm{m\,s^{-1}}$), although the differences to the other low-velocity rock types are small (black schist: 5550 $\mathrm{m\,s^{-1}}$; mica schist: 5630 $\mathrm{m\,s^{-1}}$) and the uncertainties of the mean velocities are high. In addition to its high elastic anisotropy, talc exhibits a very high $v_\mathrm{P}/v_\mathrm{S}$ ratio (e.g. Peng et al., 2022; Chen et al., 2023). This implies that the observed difference on the measured v_P values is larger for the associated v_S values. Since Rayleigh waves are more sensitive to S-wave properties, the significant difference in v_S between talc and mica schist explains the low Rayleigh-wave velocities observed on the formation with respect to its surrounding.

Another possible factor contributing to the slower velocities is the deformation and faulting history in the area, which has also been suggested as a cause for the mottled seismic reflections observed in the area (Kukkonen et al., 2012).

In addition to the geological interpretation of the observations, we evaluate the phase velocity distributions in relation to a v_P model by Singh et al. (2019) derived from first-arrival tomography of active-source data. In Figure 6, the median-filtered phase velocity map at 6 Hz is illustrated together with contour lines that indicate the corresponding depth sensitivity at each location, obtained using the $\lambda/3$ rule of thumb for the relation between horizontal wavelength λ and sensitivity depth. Across the study area, the sensitivity depth ranges from approximately 150 to 225 m. Figure 6b shows the v_P model at 140 m depth to examine the lateral velocity variation within and around the Kylylahti formation. To the first order, the position and distribution of low-velocity regions in the 6 Hz map ($< 3\,\mathrm{km\,s^{-1}}$), which correspond to depths of approximately 150-160 m, show good

https://doi.org/10.5194/egusphere-2026-4298
Preprint. Discussion started: 11 August 2026

agreement with the low-velocity zones in the v_P model depth slice, which are associated with the Kylylahti formation (Singh et al., 2019).

We obtained our Rayleigh-wave phase velocity maps using 2D Bessel function models that account for the anisotropic background illumination (Tsarsitalidou et al., 2026). While the Bessel-function parameterization in Eq. (1) describes the Green's function estimated from a wavefield excited by far-field sources (Nakahara, 2006), it does not account for the effect of the isolated sources within the array including the mining area or the scattering lithological boundaries. The dataset can thus be tested against more complicated SPAC solutions considering the Green's tensor in the near field (Haney and Nakahara, 2014), which can potentially further improve the image quality and reduce the errors.

The correlation amplitude patterns indicate a complex regional wavefield anatomy (Sect. 3, Fig. 2). The patterns resolve the target Rayleigh waves and three additional components: surface waves excited by a distant open-pit mine, and surface waves and air waves associated with blasts and the ventilation system of the Kylylahti mining activity, respectively. These wavefield components were also described by Chamarczuk et al. (2019b) using a machine learning approach and by Chamarczuk et al. (2022) using beamforming. This shows that these dominant components can consistently be identified using different processing techniques. Chamarczuk et al. (2021) and Chamarczuk et al. (2022) demonstrated that selecting only time segments dominated by body-wave energy can improve passive reflection imaging. This suggests that selecting only time segments characterized by diffuse surface-wave energy could improve passive surface-wave imaging. Alternatively, the regular dense array supports filtering techniques such as f-k analysis to optimize the reconstructed surface-wave component by removing mining induced body-wave and airwave energy based on their apparent velocities Chamarczuk et al. (2022).

The two arrivals originating from the mine are within near-field distances, i.e., the mine acts as an isolated source that is located within the array and not at far-field distances. Isolated sources within the array (Zeng and Ni, 2010) can bias the velocity estimation in ambient noise tomography (Schippkus et al., 2022), because they produce spurious arrivals. The isolated source effect of the mining activity here differs from the fault zone environment signature observed in the focal spot imaging application of Hillers et al. (2016). A passive scatterer, like a fault zone, acts as a secondary source and reflects energy that creates coda waves which are part of the Green's function (Yang et al., 2022). In contrast, the persistent and localized energy originating from the mine breaks the basic assumption of seismic interferometry, which requires seismic energy to be homogeneously and uniformly distributed within the array, and this break causes the emergence of spurious phases in the correlograms.

The array aperture allows us to reconstruct complete focal spots at a distance of 1λ and estimate the phase velocity at frequencies as low as 2 Hz. However, we exclude frequencies below 3 Hz from our analysis because the resulting velocity maps exhibit non-realistic features that are clearly associated with a wavefield generated by the mine. Above 3 Hz, this effect is no longer dominant and the velocity maps recover the Kylylahti formation, consistent with the geological model. We notice that stations close to the mine exhibit higher RSS estimates, for example at 4.5 Hz a ring-shaped pattern is formed centred at approximately $62.86°$ N, $29.33°$ E. As shown in Fig. 2, this location coincides with the source of surface waves generated by the mine. This near-field source issue is common in high-frequency ambient-noise imaging in urban environments, where sources are often located within or very close to the array (e.g., Schippkus et al., 2022). In contrast, the dispersion analysis based on longer-period surface waves are generally unaffected by this issue, as the dominant sources are located outside the

https://doi.org/10.5194/egusphere-2026-4298
Preprint. Discussion started: 11 August 2026

deployment area, typically in coastal regions for microseisms or in the open ocean for seismic hum (Nakata et al., 2019, Chapter 1).

The dense wavefield sampling facilitated by the array allows us to implement focal spot imaging using data from a distance range of 1λ around the origin, in contrast to the previous continental-scale applications where longer distances were required to provide robust velocity estimates. As the lateral resolution depends on the data range (Giammarinaro et al., 2024), we find that the short 1λ range is sufficient to obtain images that resolve the Kylylahti formation from its surrounding environment. While employing shorter data ranges can improve the resolution, the uncertainties of the velocity estimate are correspondingly higher (Tsarsitalidou et al., 2024). Using synthetic experiments Kolehmainen et al. (2025) showed that the application of a deblurring algorithm to the resulting images of the focal spot phase velocity maps can produce sharper imaging results by deconvolving the averaging effect of the finite distance ranges. This has implications for improving the image quality in future mineral exploration imaging studies where sharp lithological boundaries are expected.

Our study indicates that the focal spot method is capable of imaging hardrock subsurface structures even under non-optimal survey designs and in the presence of strong interfering sources. From a mineral exploration perspective, this suggests that the method provides a useful imaging tool for realistic exploration environments where ambient wavefield conditions are rarely compatible with the theoretical assumptions. The focal spot phase velocity maps, together with potential depth inversion models derived from them, provide a relatively low-cost and logistically easy approach to guide borehole surveys during early-stage greenfield exploration. The main benefits over more widely used ambient noise tomography are inversion-free imaging and theoretical depth resolution provided by the focal spot method. Since the resolution of the method is largely dependent on array aperture and density, an important advantage of the method is its scalability, which allows a flexible trade off between the array geometry and resolution. Greenfield exploration can be conducted using a sparse station spacing across a large area, that can then be densified in target areas of interest.

Focal spot method is suitable both as a standalone imaging technique and as part of integrated geophysical surveys and analyses. Previous studies have demonstrated the value of combining ambient seismic noise methods with active seismic surveys to extend the depth resolution (Da Col et al., 2020). Ambient noise data have also been integrated with other geophysical datasets, including gravity (Guo et al., 2025), electromagnetic (Ryberg et al., 2022) and magnetotelluric measurements (Wu et al., 2022), to enhance the depth resolution and geological interpretation.

7 Conclusions

This study presents the first application of the focal spot imaging method in a hardrock environment, using a dense-array seismic dataset recorded to characterize the Kylylahti polymetallic mineralization. The one-month dataset is preprocessed and cross-correlated following established noise imaging approaches. Rayleigh-wave phase velocities in the range of 3 to 6 Hz are estimated by parameterizing focal spots, the zero lag-time amplitude distribution, using a Bessel-function model adapted to account for anisotropic background illumination. Although mining activities during the deployment generate coherent arrivals that disrupt the symmetry of the correlation wavefield and affect the shape of the focal spots, the Bessel-function parameteriza-

https://doi.org/10.5194/egusphere-2026-4298
Preprint. Discussion started: 11 August 2026

tion up to a distance of 1λ provides robust phase velocity estimates. These estimates, verified through the RSS and the standard error, are consistent with previous subsurface imaging results at a depth of ~ 150 m.

Code and data availability. The raw continuous records from the Kylylahti array are available from Chamarczuk (2021). The software used to process the continuous data can be accessed from Boué and Stehly (2022). The Python code for implementing focal spot imaging can be obtained from Giammarinaro and Hillers (2022).

Author contributions. GH, CT, and VH conceptualized the study. GH, CT, BG, PB, LS, and VH developed the methodology. PB, LS, BG, YL, KauKol, CT, and VH developed the software used in the study. CT and VH conducted the investigation and performed the formal analysis. CT and VH were responsible for visualization. SH, MM, and KarKom curated the data. CT and VH wrote the original draft of the manuscript. GH, PB, SH, YL, and MM reviewed and edited the manuscript. GH, SH, MM, and YL supervised the research. GH and CT administered the project and acquired funding.

Competing interests. We declare that one of the co-authors is a member of the editorial board of Solid Earth.

Acknowledgements. We acknowledge the University of Helsinki IT4Science team for their support, and the computational and data storage resources of the Finnish Grid and Cloud Infrastructure (FGCI, urn:nbn:fi:research-infras-2016072533). This work was supported by the Research Council of Finland (Flagship of Advanced Mathematics for Sensing Imaging and Modeling grant 359182 and grant 322421). CT acknowledges support from the Finnish Academy of Science and Letters.

https://doi.org/10.5194/egusphere-2026-4298
Preprint. Discussion started: 11 August 2026

References

Aki, K.: Space and time spectra of stationary stochastic waves, with special reference to microtremors, Bull. Earthquake Res. Inst. Univ. Tokyo, 35, 415–457, 1957.

Alcalde, J., Carbonell, R., Pospiech, S., Gil, A., Bullock, L. A., and Tornos, F.: Preface: State of the art in mineral exploration, Solid Earth, 13, 1161–1168, https://doi.org/10.5194/se-13-1161-2022, 2022.

Asten, M. W. and Hayashi, K.: Application of the Spatial Auto-Correlation Method for Shear-Wave Velocity Studies Using Ambient Noise, Surv. Geophys., 39, 633–659, https://doi.org/10.1007/s10712-018-9474-2, 2018.

Bailey, E. and Holloway, J. R.: Experimental determination of elastic properties of talc to 800°C, 0.5 GPa; calculations of the effect on hydrated peridotite, and implications for cold subduction zones, Earth Planet. Sci. Lett., 183, 487–498, https://doi.org/https://doi.org/10.1016/S0012-821X(00)00288-0, 2000.

Boué, P. and Stehly, L.: Pycorr (v1.0) [Software], https://doi.org/10.5281/zenodo.6793401, 2022.

Catheline, S., Benech, N., Brum, J., and Negreira, C.: Time Reversal of Elastic Waves in Soft Solids, Phys. Rev. Lett., 100, 064 301, https://doi.org/10.1103/PhysRevLett.100.064301, 2008.

Chamarczuk, M.: Kylylahti 3D virtual seismic survey (unprocessed ambient-noise recordings), https://doi.org/10.23729/48acb337-3be0-4e76-94f9-5e60779c26fe, institute of Geophysics PAS, 2021.

Chamarczuk, M., Malinowski, M., Nishitsuji, Y., Thorbecke, J., Koivisto, E., Heinonen, S., Juurela, S., Mężyk, M., and Draganov, D.: Automatic 3D illumination-diagnosis method for large-N arrays: Robust data scanner and machine-learning feature provider, Geophysics, 84, Q13–Q25, https://doi.org/10.1190/geo2018-0504.1, 2019a.

Chamarczuk, M., Nishitsuji, Y., Malinowski, M., and Draganov, D.: Unsupervised Learning Used in Automatic Detection and Classification of Ambient-Noise Recordings from a Large-N Array, Seismol. Res. Lett., 91, 370–389, https://doi.org/10.1785/0220190063, 2019b.

Chamarczuk, M., Malinowski, M., and Draganov, D.: 2D body-wave seismic interferometry as a tool for reconnaissance studies and optimization of passive reflection seismic surveys in hardrock environments, J. Appl. Geophys., 187, 104 288, https://doi.org/https://doi.org/10.1016/j.jappgeo.2021.104288, 2021.

Chamarczuk, M., Malinowski, M., Draganov, D., Koivisto, E., Heinonen, S., and Rötsä, S.: Reflection imaging of complex geology in a crystalline environment using virtual-source seismology: case study from the Kylylahti polymetallic mine, Finland, Solid Earth, 13, 705–723, https://doi.org/10.5194/se-13-70, 2022.

Chen, P., Wang, D., Cai, N., Zhang, J., Zhang, R., and Cao, Y.: Anomalous Sound Velocities of Talc at High Pressure and Implications for Estimating Water Content in Mantle Wedge, J. Geophys. Res. Solid Earth, 128, e2023JB027 309, https://doi.org/https://doi.org/10.1029/2023JB027309, e2023JB027309 2023JB027309, 2023.

Colombero, C., Papadopoulou, M., Kauti, T., Skyttä, P., Koivisto, E., Savolainen, M., and Socco, L. V.: Surface-wave tomography for mineral exploration: a successful combination of passive and active data (Siilinjärvi phosphorus mine, Finland), Solid Earth, 13, 417–429, https://doi.org/10.5194/se-13-417-2022, 2022.

Da Col, F., Papadopoulou, M., Koivisto, E., Sito, , Savolainen, M., and Socco, L. V.: Application of surface-wave tomography to mineral exploration: a case study from Siilinjärvi, Finland, Geophys. Prospect., 68, 254–269, https://doi.org/https://doi.org/10.1111/1365-2478.12903, 2020.

Derode, A., Larose, E., Campillo, M., and Fink, M.: How to estimate the Green's function of a heterogeneous medium between two passive sensors? Application to acoustic waves, Appl. Phys. Lett., 83, 3054–3056, https://doi.org/10.1063/1.1617373, 2003a.

Derode, A., Larose, E., Tanter, M., de Rosny, J., Tourin, A., Campillo, M., and Fink, M.: Recovering the Green's function from field-field correlations in an open scattering medium (L), J. Acoust. Soc. Am., 113, 2973–2976, https://doi.org/10.1121/1.1570436, 2003b.

Ekström, G.: Love and Rayleigh phase-velocity maps, 5–40 s, of the western and central USA from USArray data, Earth Planet. Sci. Lett., 402, 42–49, https://doi.org/10.1016/j.epsl.2013.11.022, special issue on USArray science, 2014.

Fink, M.: Time-reversed acoustics, Sci. Am., 281, 91–97, 1999.

Foti, S., Hollender, F., Garofalo, F., Albarello, D., Asten, M., Bard, P., Comina, C., Cornou, C., Cox, B., Di Giulio, G., Forbriger, T., Hayashi, K., Lunedei, E., Martin, A., Mercerat, D., Ohrnberger, M., Poggi, V., Renalier, F., Sicilia, D., and Socco, V.: Guidelines for the good practice of surface wave analysis: a product of the InterPACIFIC project, Bull. Earthq. Eng., 16, 2367–2420, https://doi.org/10.1007/s10518-017-0206-7, 2018.

Giammarinaro, B. and Hillers, G.: Resources for seismic surface wave focal spot imaging: numerical resolution experiments [Software], https://doi.org/10.23729/61e3eefb-e7ce-44af-8fc3-01cac0bbba0d, 2022.

Giammarinaro, B., Tsarsitalidou, C., Hillers, G., de Rosny, J., Seydoux, L., Catheline, S., Campillo, M., and Roux, P.: Seismic surface wave focal spot imaging: numerical resolution experiments, Geophys. J. Int., 232, 201–222, https://doi.org/10.1093/gji/ggac247, 2023.

Giammarinaro, B., Tsarsitalidou, C., and Hillers, G.: Investigating the lateral resolution of the Rayleigh wave focal spot imaging technique using two-dimensional acoustic simulations, C. R. Geosci., 356, 41–57, https://doi.org/10.5802/crgeos.254, 2024.

Guo, L., Bao, X., Shen, Y., Chen, Y., and Han, M.: Joint inversion of full-waveform ambient noise and gravity data for simultaneously deriving high-resolution three-dimensional crustal S-wave velocity and density models: application to the Jingpohu volcanic area in Northeast China, Geophys. J. Int., 240, 1168–1180, https://doi.org/10.1093/gji/ggae434, 2025.

Haney, M. M. and Nakahara, H.: Surface-Wave Green's Tensors in the Near Field, Bull. Seismol. Soc. Am., 104, 1578–1586, https://doi.org/10.1785/0120130113, 2014.

Haney, M. M., Mikesell, T. D., van Wijk, K., and Nakahara, H.: Extension of the spatial autocorrelation (SPAC) method to mixed-component correlations of surface waves, Geophys. J. Int., 191, 189–206, https://doi.org/https://doi.org/10.1111/j.1365-246X.2012.05597.x, 2012.

Hayashi, K., Asten, M. W., Stephenson, W., Cornou, C., Hobiger, M., Pilz, M., and Yamanaka, H.: Microtremor array method using spatial autocorrelation analysis of Rayleigh-wave data, J. Seismol., 2022.

Heinonen, S., Malinowski, M., Hloušek, F., Gislason, G., Buske, S., Koivisto, E., and Wojdyla, M.: Cost-Effective Seismic Exploration: 2D Reflection Imaging at the Kylylahti Massive Sulfide Deposit, Finland, Minerals, 9, https://doi.org/10.3390/min9050263, 2019.

Hillers, G., Roux, P., Campillo, M., and Ben-Zion, Y.: Focal spot imaging based on zero lag cross-correlation amplitude fields: Application to dense array data at the San Jacinto fault zone, J. Geophys. Res. Solid Earth, 121, 8048–8067, https://doi.org/10.1002/2016JB013014, 2016.

Koivisto, E. A.-L., Malinowski, M., Heinonen, S., Cosma, C., Wojdyla, M., Vaittinen, K., Chamarczuk, M., Riedel, M., Kukkonen, I. T., and Group, C.-M. W.: From Regional Seismics to High-Resolution Resource Delineation: Example from the Outokumpu Ore District, Eastern Finland, in: Proceedings of the 2nd Conference on Geophysics for Mineral Exploration and Mining, EAGE Near Surface Geoscience Conference & Exhibition 2018, https://doi.org/10.3997/2214-4609.201802716, 2018.

Kolehmainen, K., Hillers, G., Giammarinaro, B., Juvonen, M., Meaney, A., and Siltanen, S.: Estimation of the seismic focal spot imaging point spread function, EGU General Assembly 2025, Vienna, Austria, https://doi.org/10.5194/egusphere-egu25-6164, 2025.

Kontinen, A., Peltonen, P., and Huhma, H.: Description and genetic modelling of the Outokumpu-type rock assemblage and associated sulphide deposits, Report M10.4/2006/1, Geol. Surv. of Fin., 2006.

Kukkonen, I., Heikkinen, P., Heinonen, S., Laitinen, J., and Sorjonen-Ward, P.: HIRE Seismic Reflection Survey in the Outokumpu-Polvijärvi Cu-Co-Zn Mining and Exploration Area, Eastern Finland, Report 55/2012, Geol. Surv. of Fin., 2012.

Kästle, E. D., El-Sharkawy, A., Boschi, L., Meier, T., Rosenberg, C., Bellahsen, N., Cristiano, L., and Weidle, C.: Surface Wave Tomography of the Alps Using Ambient-Noise and Earthquake Phase Velocity Measurements, J. Geophys. Res. Solid Earth, 123, 1770–1792, https://doi.org/10.1002/2017JB014698, 2018.

Li, Y., Clayton, R. W., and Villa, V.: Mapping the near-field scattered energy in sedimentary basins from ambient noise correlations, Geophys. J. Int., 242, ggaf170, https://doi.org/10.1093/gji/ggaf170, 2025.

Luhta, T.: Petrophysical properties of the Kylylahti Cu-Au-Zn sulphide mineralization and its host rocks, Master's thesis, University of Helsinki, 2018.

Mainprice, D., Le Page, Y., Rodgers, J., and Jouanna, P.: Ab initio elastic properties of talc from 0 to 12GPa: Interpretation of seismic velocities at mantle pressures and prediction of auxetic behaviour at low pressure, Earth Planet. Sci. Lett., 274, 327–338, https://doi.org/https://doi.org/10.1016/j.epsl.2008.07.047, 2008.

Nakahara, H.: A systematic study of theoretical relations between spatial correlation and Green's function in one-, two- and three-dimensional random scalar wavefields, Geophys. J. Int., 167, 1097–1105, 2006.

Nakata, N., Gualtieri, L., and Fichtner, A.: Seismic Ambient Noise, Cambridge University Press, https://doi.org/10.1017/9781108264808, 2019.

Okada, H. and Suto, K.: The Microtremor Survey Method, Society of Exploration Geophysicists, https://doi.org/10.1190/1.9781560801740, 2003.

Pedregosa, F., Varoquaux, G., Gramfort, A., Michel, V., Thirion, B., Grisel, O., Blondel, M., Prettenhofer, P., Weiss, R., Dubourg, V., Vanderplas, J., Passos, A., Cournapeau, D., Brucher, M., Perrot, M., and Duchesnay, E.: Scikit-learn: Machine Learning in Python, J. Mach. Learn. Res., 12, 2825–2830, 2011.

Peltonen, P., Kontinen, A., Huhma, H., and Kuronen, U.: Outokumpu revisited: New mineral deposit model for the mantle peridotite-associated Cu–Co–Zn–Ni–Ag–Au sulphide deposits, Ore Geol. Rev., 33, 559–617, https://doi.org/https://doi.org/10.1016/j.oregeorev.2007.07.002, 2008.

Peng, Y., Mookherjee, M., Hermann, A., Manthilake, G., and Mainprice, D.: Anomalous elasticity of talc at high pressures: Implications for subduction systems, Geosci. Front., 13, 101 381, https://doi.org/https://doi.org/10.1016/j.gsf.2022.101381, 2022.

Riedel, M., Cosma, C., Enescu, N., Koivisto, E., Komminaho, K., Vaittinen, K., and Malinowski, M.: Underground Vertical Seismic Profiling with Conventional and Fiber-Optic Systems for Exploration in the Kylylahti Polymetallic Mine, Eastern Finland, Minerals, 8, https://doi.org/10.3390/min8110538, 2018.

Ryberg, T., Kirsch, M., Haberland, C., Tolosana-Delgado, R., Viezzoli, A., and Gloaguen, R.: Ambient seismic noise analysis of LARGE-N data for mineral exploration in the Central Erzgebirge, Germany, Solid Earth, 13, 519–533, https://doi.org/10.5194/se-13-519-2022, 2022.

Schippkus, S., Snieder, R., and Hadziioannou, C.: Seismic interferometry in the presence of an isolated noise source, Seismica, 1, https://doi.org/10.26443/seismica.v1i1.195, 2022.

Seydoux, L., de Rosny, J., and Shapiro, N. M.: Pre-processing ambient noise cross-correlations with equalizing the covariance matrix eigenspectrum, Geophys. J. Int., 210, 1432–1449, 2017.

Singh, B., Malinowski, M., Hloušek, F., Koivisto, E., Heinonen, S., Hellwig, O., Buske, S., Chamarczuk, M., and Juurela, S.: Sparse 3D Seismic Imaging in the Kylylahti Mine Area, Eastern Finland: Comparison of Time Versus Depth Approach, Minerals, 9, https://doi.org/10.3390/min9050305, 2019.

Sánchez-Sesma, F. J. and Campillo, M.: Retrieval of the Green's Function from Cross Correlation: The Canonical Elastic Problem, Bull. Seismol. Soc. Am., 96, 1182–1191, https://doi.org/10.1785/0120050181, 2006.

Tsai, V. C. and Moschetti, M. P.: An explicit relationship between time-domain noise correlation and spatial autocorrelation (SPAC) results, Geophys. J. Int., 182, 454–460, https://doi.org/10.1111/j.1365-246X.2010.04633.x, 2010.

Tsarsitalidou, C., Hillers, G., Giammarinaro, B., Boué, P., Stehly, L., and Campillo, M.: Long period Rayleigh wave focal spot imaging applied to USArray data, J. Geophys. Res. Solid Earth, 129, e2023JB027 417, https://doi.org/https://doi.org/10.1029/2023JB027417, 2024.

Tsarsitalidou, C., Hillers, G., Stehly, L., Giammarinaro, B., Boué, P., and Paul, A.: Rayleigh-wave focal spot imaging of the European Alps and surrounding areas, Geophys. J. Int., https://doi.org/10.1093/gji/ggag017, 2026.

Wapenaar, K., Draganov, D., Snieder, R., Campman, X., and Verdel, A.: Tutorial on seismic interferometry. Part I: Basic principles and applications, Geophysics, 75, 75A195–75 209, https://doi.org/10.1190/1.3457445, 2010.

Wilczynski, Z., Kaslilar, A., Malehmir, A., Manzi, M., Vivin, L., Lepine, J., Valishin, O., and Högdahl, K.: Ambient noise surface-wave imaging in a hardrock environment: implications for mineral exploration, Geophys. J. Int., 240, 571–590, https://doi.org/10.1093/gji/ggae392, 2024.

Wu, P., Tan, H., Ding, Z., Kong, W., Peng, M., Wang, X., and Xu, L.: Joint inversion of 3-D magnetotelluric and ambient noise dispersion data sets with cross-gradient constraints: methodology and application, Geophys. J. Int., 230, 714–732, https://doi.org/10.1093/gji/ggac049, 2022.

Yang, Y., Zhan, Z., Shen, Z., and Atterholt, J.: Fault Zone Imaging With Distributed Acoustic Sensing: Surface-To-Surface Wave Scattering, J. Geophys. Res. Solid Earth, 127, e2022JB024 329, https://doi.org/https://doi.org/10.1029/2022JB024329, 2022.

Zeng, X. and Ni, S.: A persistent localized microseismic source near the Kyushu Island, Japan, Geophys. Res. Lett., 37, https://doi.org/https://doi.org/10.1029/2010GL045774, 2010.

https://doi.org/10.5194/egusphere-2026-4298
Preprint. Discussion started: 11 August 2026

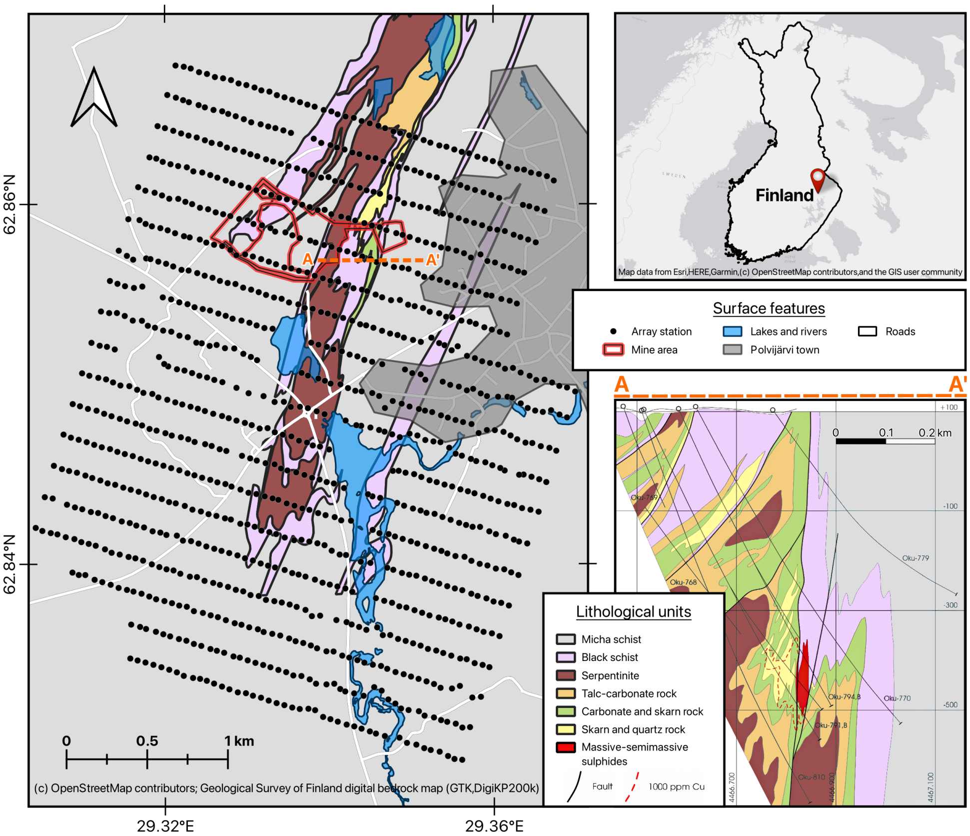

Figure 1. The geometry of the 10.5 km^2 Kylylahti dense seismic array together with a stylized geological map and selected surface features. A-A' is a cross-section through the Kylylahti deposit, modified from Peltonen et al. (2008).

https://doi.org/10.5194/egusphere-2026-4298
Preprint. Discussion started: 11 August 2026

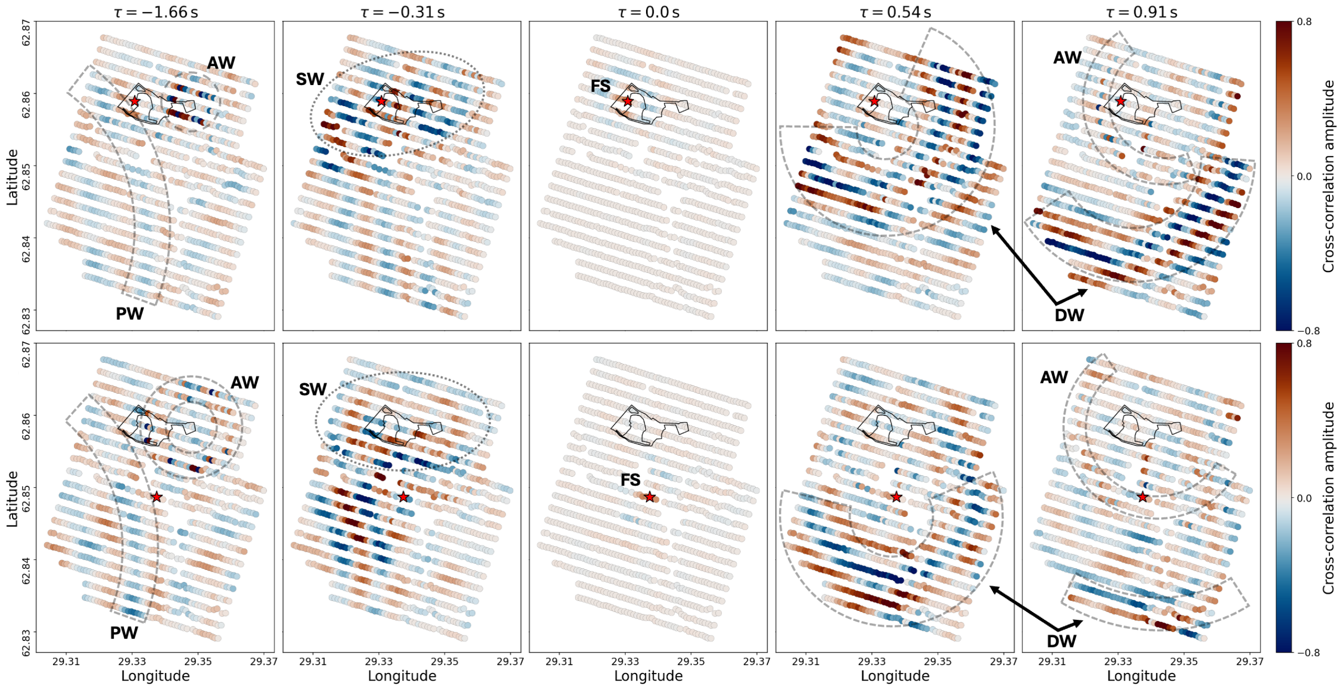

Figure 2. Snapshots of correlation wavefields at five different lag times associated with reference stations 516 (upper row) and 1029 (lower row) indicated by the red star. Correlations are calculated from the continuous records of 30 days and bandpass filtered from $3-6$ Hz. Reconstructed features include an acoustic wave excited by mine ventilation (AW), plane waves originating from a distant open pit mine to the SW (PW), surface waves excited by mine activity (SW), a broadband Rayleigh-wave focal spot (FS), and a diverging wavefront (DW) excited at the virtual source locations. The limits of the underground mine facilities at the surface are indicated by the contour in the upper left quadrant. Amplitudes are normalized independently in each panel and are clipped at ± 0.8, which leads to the variable relative strength of the indicated features across the sequences.

https://doi.org/10.5194/egusphere-2026-4298
Preprint. Discussion started: 11 August 2026

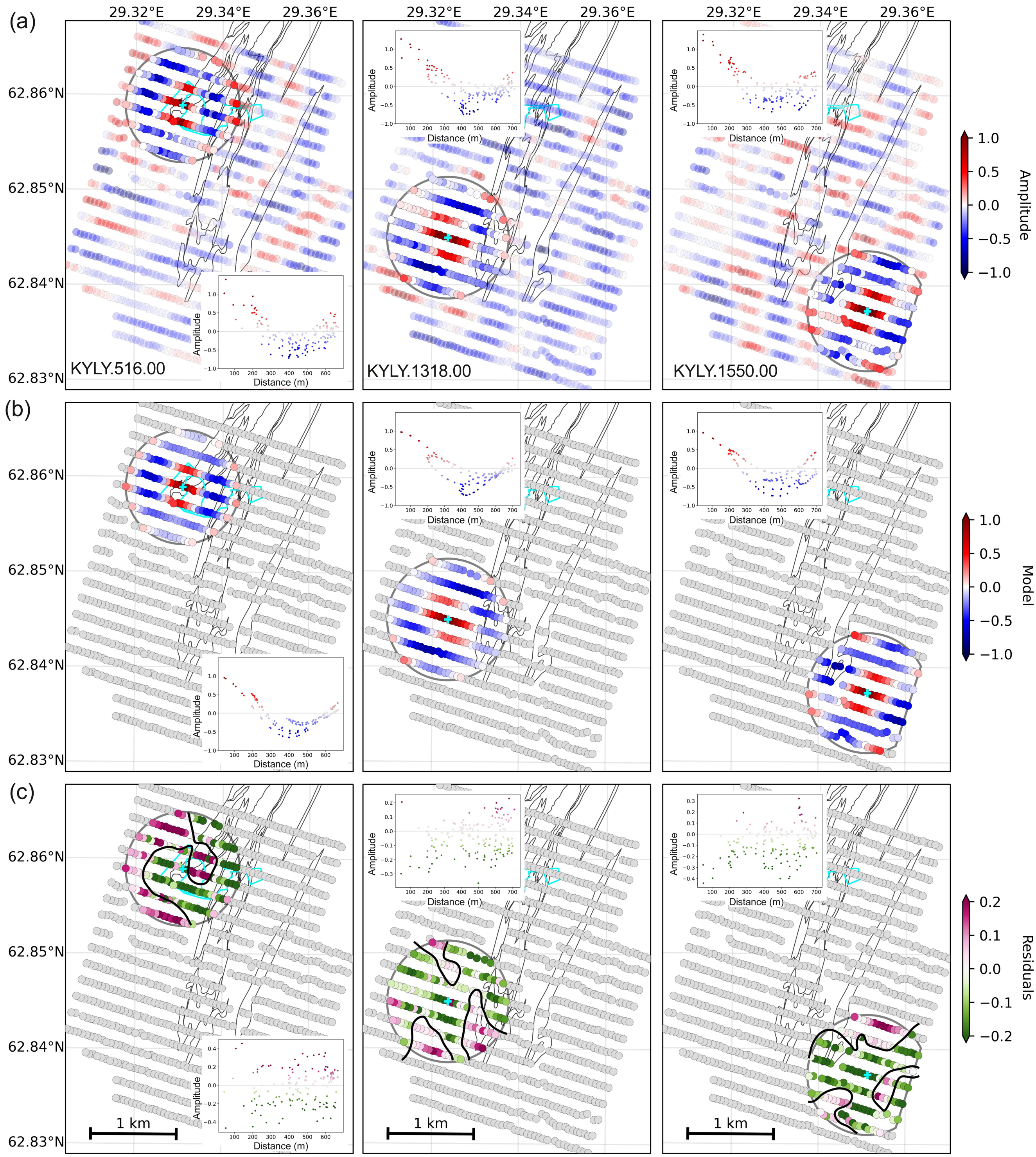

Figure 3. (a) Rayleigh-wave spatial autocorrelation fields or focal spots narrow-band filtered at 4 Hz for three stations with code names 516, 1318, and 1550. (b) The associated focal spot model amplitude using the parametrization described in Sect. 4. (c) The residuals are the difference between the focal spot model and data amplitudes. The insets indicate the associated amplitude distributions as a function of radial distance. The mine area is outlined with cyan color. The grey circle indicates the 1λ distance from the reference station. The contour paths in (c) are drawn to highlight the negative and positive value pattern.

https://doi.org/10.5194/egusphere-2026-4298
Preprint. Discussion started: 11 August 2026

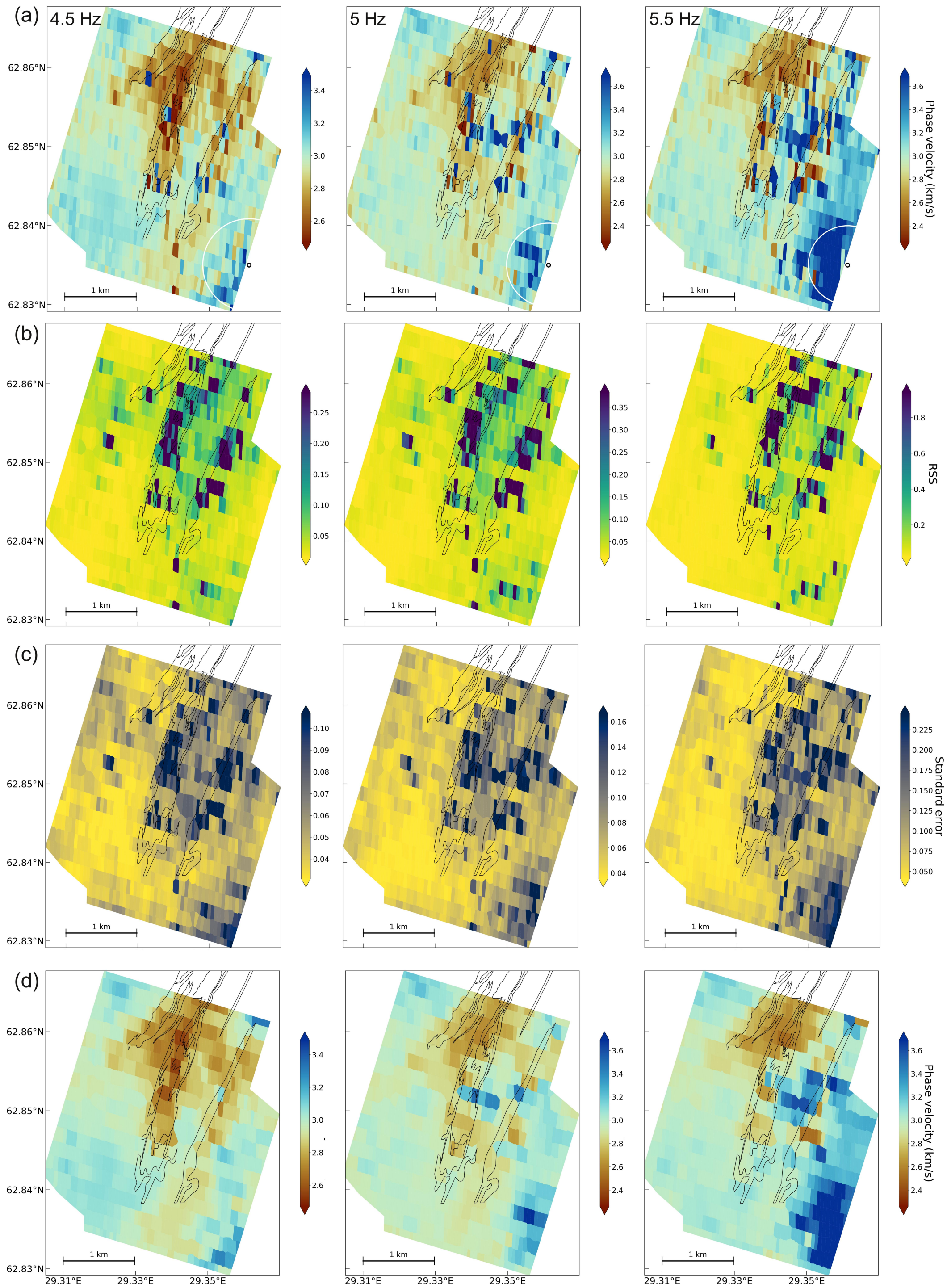

Figure 4. (a) Focal spot based Rayleigh-wave phase velocity maps at 4.5, 5, and 5.5 Hz estimated by the procedure discussed in Sect. 4. The white half-circle in the lower right corner indicates the 1λ distance around a reference station. (b) RSS maps obtained from the residuals between the focal spot data and the associated model. (c) Standard error maps distributions. (d) Median-filtered version of the phase velocity distributions in panel (a).

https://doi.org/10.5194/egusphere-2026-4298
Preprint. Discussion started: 11 August 2026

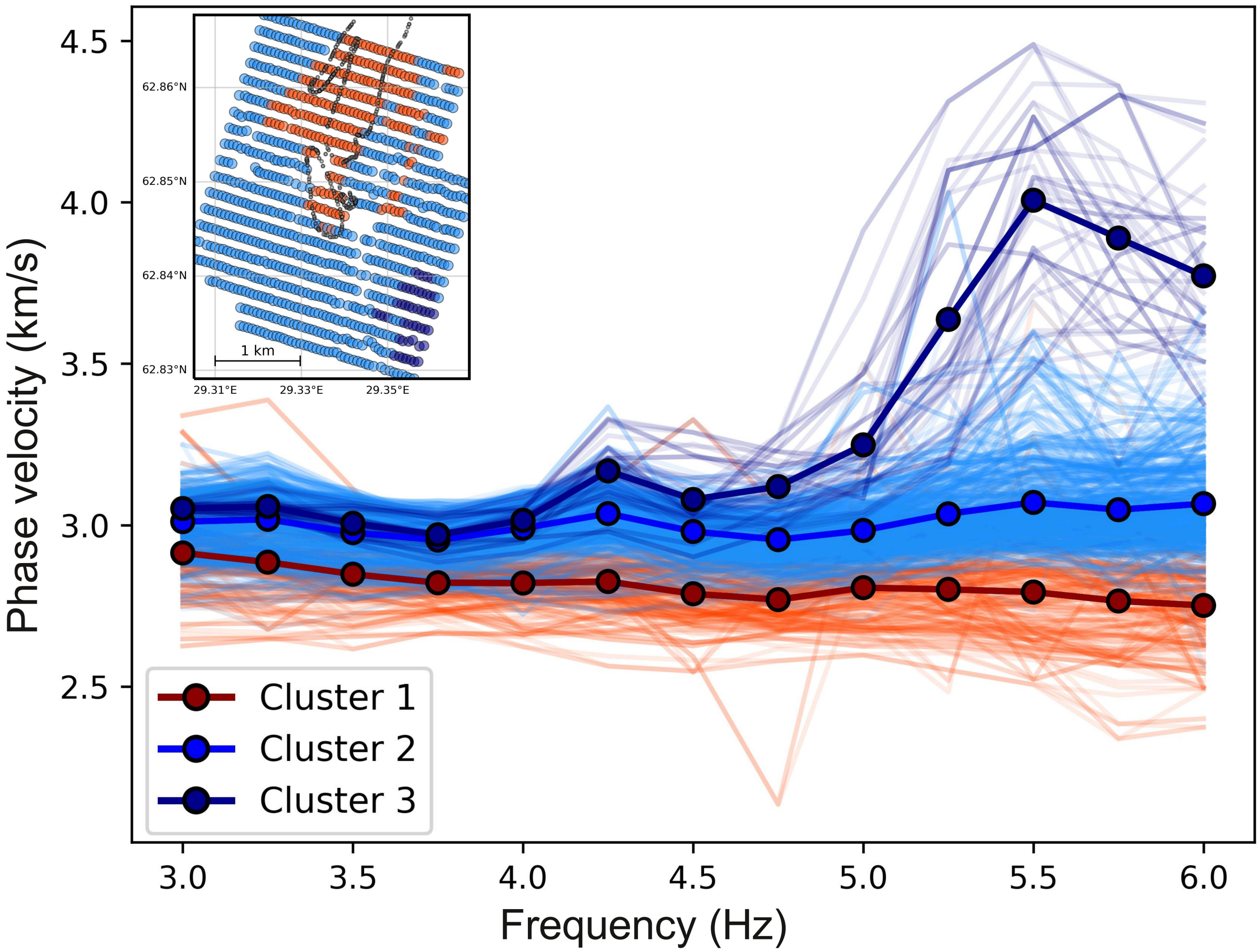

Figure 5. Results of the dispersion-curve clustering described in Sect. 5.3. Each dispersion curve is color-coded by cluster. The cluster average dispersion curves are shown by the heave line. Circles highlight the 0.25 Hz sampling. The inset map shows station locations colored according to their associated cluster. The black dots delineate the boundaries of the Kylylahti formation at 150 m depth obtained from the geological model provided by the Boliden mining company.

https://doi.org/10.5194/egusphere-2026-4298
Preprint. Discussion started: 11 August 2026

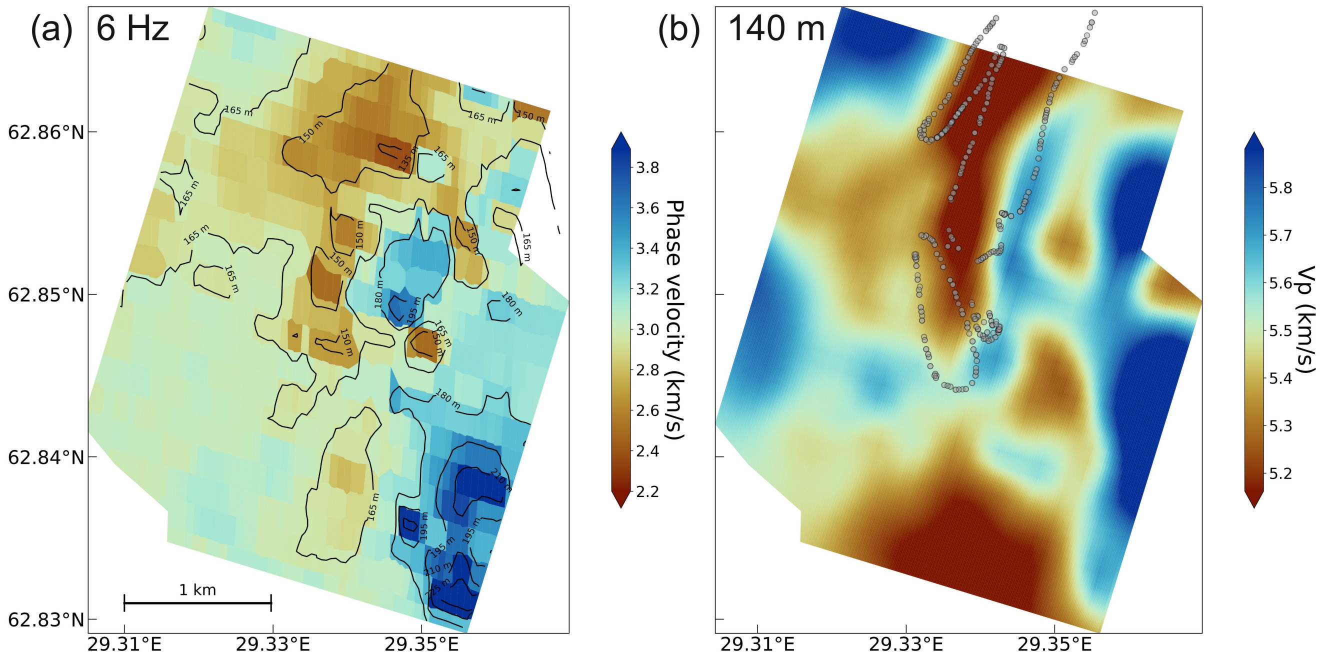

Figure 6. (a) Rayleigh-wave phase velocity map at 6 Hz. The contour lines indicate the corresponding sensitivity depth at each location estimated from the $\lambda/3$ rule of thumb. (b) The v_P model of Singh et al. (2019) together with the outline of the Kylylahti formation from the Boliden geological model at 140 m depth.